ANNALS OF GEOPHYSICS, 68, 1, V105, 2025; doi:10.4401/ag-9134
OPEN ACCESS

3D reconstruction of volcanic bombs to enhance ballistic trajectory predictions

Marco Reale Calafino[1], Luigi Mereu[2,3], Danilo Messina[4,5], Massimo Cantarero[4], Emanuela De Beni[4], Cristina Proietti[4], Michele Prestifilippo[4], Francesca Forni[1], Simona Scollo[*,4]

(1) Università La Statale, Dipartimento di Scienze della Terra "Ardito Desio", Milano, Italia
(2) Istituto Nazionale di Geofisica e Vulcanologia, sezione di Bologna, Bologna, Italia
(3) Università de L'Aquila, Center of Excellence CETEMPS, L'Aquila, Italia
(4) Istituto Nazionale di Geofisica e Vulcanologia, Osservatorio Etneo, Catania, Italia
(5) Università di Palermo, Dipartimento di Scienze della Terra e del Mare, Palermo, Italia

Article history: received August 2, 2024; accepted January 24, 2025

Abstract

Volcanic Ballistic Projectiles (VBPs) ejected during explosive eruptions represent a significant hazard to people approaching the craters of active volcanoes. Recently, several models have been proposed to simulate the trajectories of VBPs, thus contributing to assessing the associated hazards. However, these models mostly rely on field data, which may not be readily available. Indeed, often the large size and weight of VBPs make their transportation to a laboratory for detailed physical measurements extremely challenging. This work compares different methodologies useful to extract 3D models of VBPs and measure their dimensions (length, width, and thickness) and volume. A VBP collected at Mt. Etna (Italy) after the 21 May 2023 eruption was used as a test sample. Specifically, we processed a series of images, acquired with a smartphone using two photogrammetric software, one freely available and one commercial. The 3D model of the sample was also obtained through a LiDAR sensor integrated into the smartphone. The dimensions and volume of the sample were measured using a caliper and Archimedes' principle and were used as reference values for quantifying the accuracy of the different reconstruction methodologies. We found that the commercial software is well suited to estimate size and volume, providing a high-precision reconstruction even for the irregular shape of highly porous volcanic particles (with uncertainties of <6% and 16% for the mean diameter and volume, respectively). However, we suggest that, among all the analysed methods, the LiDAR offers a good compromise in terms of accuracy (with uncertainties of <12% and <86% or the mean diameter and volume, respectively) and ease of field operations. Finally, we estimated the ballistic trajectory of VBP using the diameters estimated from the different volumes finding that the distance reached by VBP can have variations up to 350 m only due to a different way to estimate the particle size. We thus conclude that the methods investigated in this work could be applied to different volcanoes worldwide to determine the 3D shape of VBPs because incorrectly estimating the size of VBPs can bias ballistic hazard models.

Keywords: Volcanic Ballistic Projectiles; photogrammetry; shape and volume estimations, ballistic trajectory

1. Introduction

Explosive eruptions produce large quantities of volcanic particles of different sizes and compositions which pose a major threat to people living near active volcanoes and aviation operations (Blong, 1984; Guffanti et al., 2005). Volcanic particles with a size larger than 64 mm are named blocks and they can be of lithic or juvenile origin. These particles are also known as Volcanic Ballistic Projectiles (VBPs) (Taddeucci et al., 2017). Most of them fall close to the volcano's vent and up to about 10 km away from it, causing significant damage to infrastructures and the surrounding environment (Blong, 1984). Additionally, VBPs represent a risk for tourists, hikers, mountaineers, locals, and volcanologists who frequently visit the volcano summit or the vent area (Brown et al., 2017). According to Fitzgerald (2017), the fallout of VBPs has caused at least 76 recorded deaths at six different volcanoes around the world since 1993 (i.e., Galeras, Yasur, Popocatepetl, Pacaya, Raoul Island and Ontake). At Etna, two explosive events in 1929 and 1979 caused a total of 11 casualties (Chester et al., 1985; Guest et al., 1980; Kiffer, 1979; Murraey, 1980). Moreover, the fallout of VBPs has forced the closure of touristic viewpoints and trails at Stromboli, Italy, and Kilauea's Halema'uma'u, Hawaii (Taddeucci et al., 2017).

Hazard maps of VBPs rely upon both numerical modelling, aimed at reconstructing ballistic trajectories, and field data collection, able to map the spatial distribution and size of VBPs (e.g. Fitzgerald et al., 2014; Gurioli et al., 2013; Swanson et al., 2012; Cioni et al., 2024). While numerical models simulating ballistic trajectories have been extensively developed since 1940 (e.g. Minakami et al., 1942; Mastin, 2001; Tsunematsu et al., 2014), remote sensing techniques have been employed to investigate VBP deposits in the field only recently. For example, drones coupled with photogrammetry were used to quantify the size of VBPs at Yasur (Fitzgerald et al., 2020) and Stromboli (Bisson et al., 2023) volcanoes. High-resolution thermal and visible cameras were recently used to estimate particle size above the vent (Pioli et al., 2022) while high-resolution orthomosaic extracted from Unoccupied Aerial Systems (UAS) images were analyzed to assess the density map of VBPs with sizes exceeding 20 cm (Proietti et al., 2023). The 3D reconstruction of VBPs is crucial to estimate particle sizes, which in turn are used to evaluate the terminal settling velocity of volcanic particles. In fact, in a multiphase flow, the fluid-particle drag force Fd is defined as:

$$F_d = \frac{1}{2}\rho_f C_D A_p |v_p - v_f|(v_p - v_f) \tag{1}$$

where ρ_f is the fluid density, C_D is the drag coefficient, A_p is the particle surface area, and v_p, v_f are the particle and fluid velocity, respectively. A particle falling in a fluid reaches a constant velocity named terminal settling velocity w_t that can be estimated, following Dellino et al. (2005) as:

$$w_t = \sqrt{\frac{4gd_p(\rho_p - \rho_f)}{3C_D\rho_f}} \tag{2}$$

For spherical particles, the Reynolds number (Reynolds, 1883; Stokes, 1851) is defined as:

$$R_e = \frac{\rho_f w_t d_p}{\mu_f} \tag{3}$$

where μ_f is the fluid viscosity. For no spherical particles, as those erupted by volcanoes, the drag coefficient is a complex function of both R_e and shape (Ganser and Gary,1993; Bagheri and Bonadonna, 2016; Dioguardi et al., 2018). This is the reason why the estimation of the volcanic particle size and shape is very important. Several studies have focused on the estimation of shape parameters of volcanic ashes in two-dimension through scanning electron microscope (SEM) analyses (Heiken et al., 1985; Coltelli et al., 2008; Ersoy et al., 2010; Liu et al., 2015; Bonadonna et al., 2011). Up to now, 3D reconstructions of VBPs have been carried out using techniques that require transferring samples from the field to the laboratory to obtain high-resolution digital photographs of specimens mounted on a goniometric universal stage under a stereomicroscope (Dellino et al., 2005) or using X-ray computed tomographic scans (Saxby et al., 2020).

This work presents alternative methodologies that allow the reconstruction of the 3D shape of VBPs in a fast and easy way. The methods, applied to a VBP ejected during the 21/05/2023 Etna eruption (De Beni et al., 2024), include photogrammetric 3D reconstructions obtained with two different software (named VisualSfM and Agisoft Metashape) as well as the use of a LiDAR sensor integrated into the smartphone. The results of 3D reconstructions were compared and used to improve the input parameters of the ballistic model named Eject! (Mastin et al., 2001).

2. The activity of 21 May 2023

Mt. Etna is one of the most active volcanoes in Europe and has produced about 80 high lava fountains over the last three years at the time of writing (Calvari et al., 2022; Proietti et al., 2024). These episodes caused several inconveniences to the populations living on its flanks, especially due to the tephra fallout, mostly impacting the eastern side (Mereu et al., 2023), and the fallout of VPBs, which mostly affected touristic areas (Costa et al., 2023). Figure 1 shows examples of VPBs that erupted during different episodes of lava fountaining between March 2021 and October 2023, and that fell at a distance of 1-7 km from Etna's summit craters.

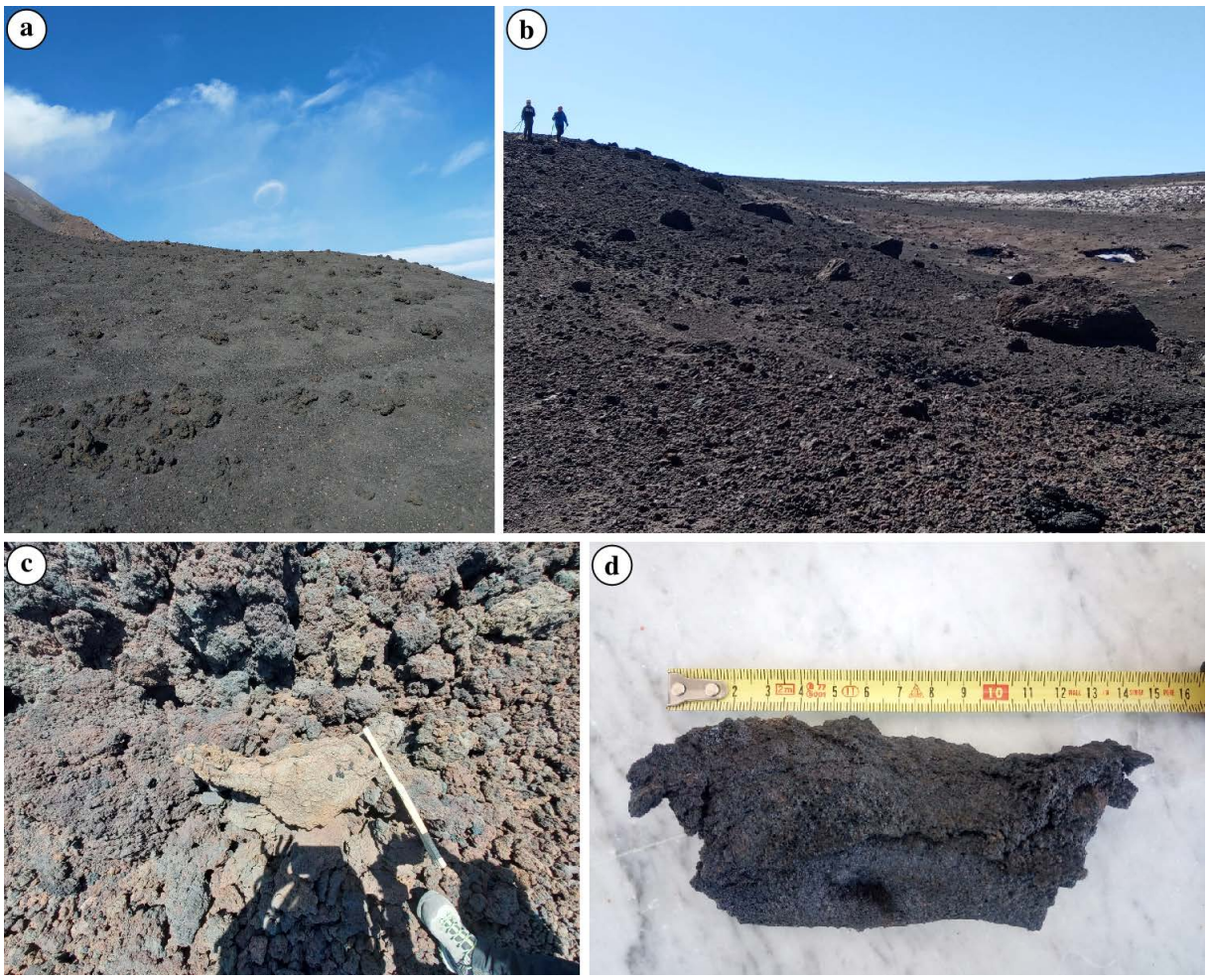

Figure 1. Photos of VBPs near Etna's summit craters were taken by S. Scollo on (a) 23 February 2022, (b) 30 October 2023, and (c) 18 June 2023, and (d) on 28 March 2021 at Mt. Rinatu, courtesy of Giò Giusa.

On 21 May 2023, an eruption from Etna's South East Crater (SEC) occurred while the volcano summit was completely invisible due to bad weather conditions (De Beni et al., 2024). This eruption produced two lava flows on the southern and eastern flanks of SEC, a volcaniclastic deposit covering the south lava flow in its middle portion, and a thin tephra deposit visible in the southwestern flank of the volcano. During this event, the international airport

of Catania, located about 30 km to the south of Etna's summit, was compelled to shut down. Fieldwork conducted in the summit area on the 19th of June 2023 revealed the presence of several VBPs deposited above the lava and the pyroclastic deposits (Fig. 2).

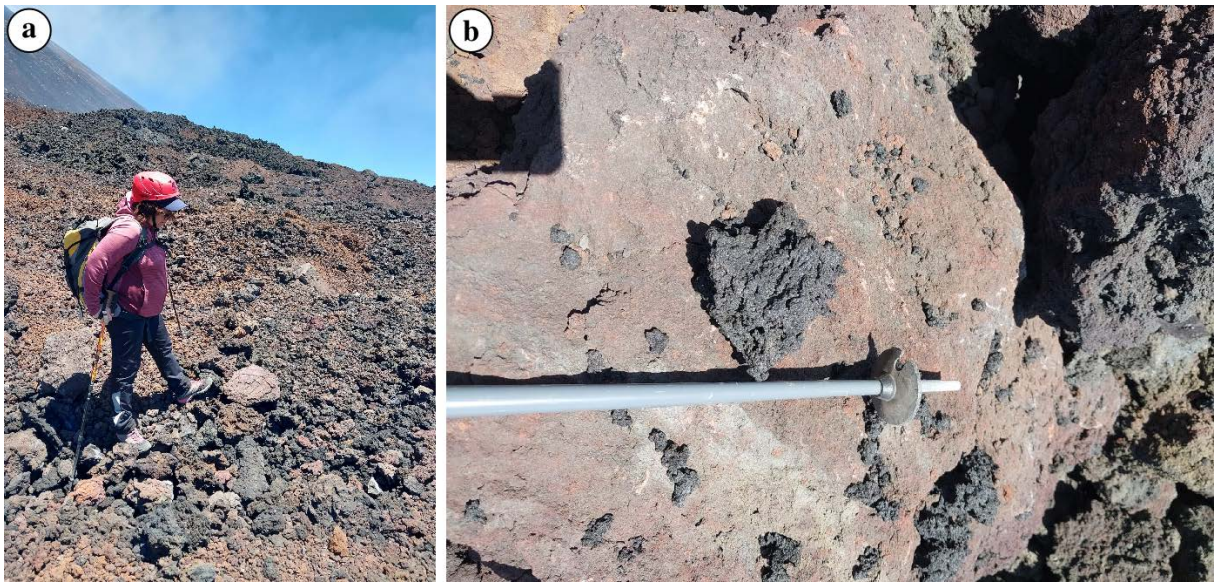

Figure 2. (a) VBPs deposited above the pyroclastic flow observed during the field survey of 19 June 2023; (b) a detail of a volcanic bomb collected in the field on 19 June 2023.

3. Method

A VBP ejected during the 21 May 2023 lava fountain event at Etna was collected at an altitude of 2857 m (lat = 37.73572°; lon = 14.998361°) and at a distance of about 1100 m from the SEC. The sample was photographed using a smartphone at INGV-OE. Additionally, the specimen was scanned with a LiDAR sensor implemented on a smartphone. To perform its 3D reconstruction, the photos were processed with two different photogrammetric softwares: VisualSfM (VSFM), a freeware tool, and Agisoft Metashape (AM). a commercial software. The linear dimensions of the sample (length = a, width = b, and thickness = c) were measured directly using a caliper. Its volume was calculated using Archimedes' principle by measuring the changes in water level in a graduated glass beaker after immersing the sample covered in waterproofing resin. The differences between the modelled and measured dimensions and volumes were used to assess the accuracy of the employed methods.

3.1 Camera Detail and Image Acquisition

Before acquiring photos of the VPB sample, an appropriate setup was arranged to avoid including foreign objects within the framing area and facilitate subsequent image processing. The sample was placed on a cardboard cylinder to minimize the portion not visible due to the supporting surface. A sheet of green paper was placed under the cylinder to enhance the colour contrast between the sample and the background. Finally, a set of graphic markers (e.g. crosses, circles, lines) was drawn on the sample (Fig. 3a). The linear distances between each pair of markers, measured with a ruler and a caliber, were used in the processing phase to estimate the scale factor between the modelled and the real particle size. To capture images of the sample from various angles, we rotated the cylinder while keeping the camera stationary and maintaining a consistent distance of about 80-100 centimeters between the sample and the camera (Fig. 3b). We acquired two sets of images using an Apple iPhone 15 pro (camera resolution 48 + 12 + 12 megapixel with a focal length of 24, 13 and 77 mm, respectively) by rotating the sample by 180° and placing it first on its long axis and then on its short axis (65 and 61 photos, respectively). Considering that it could

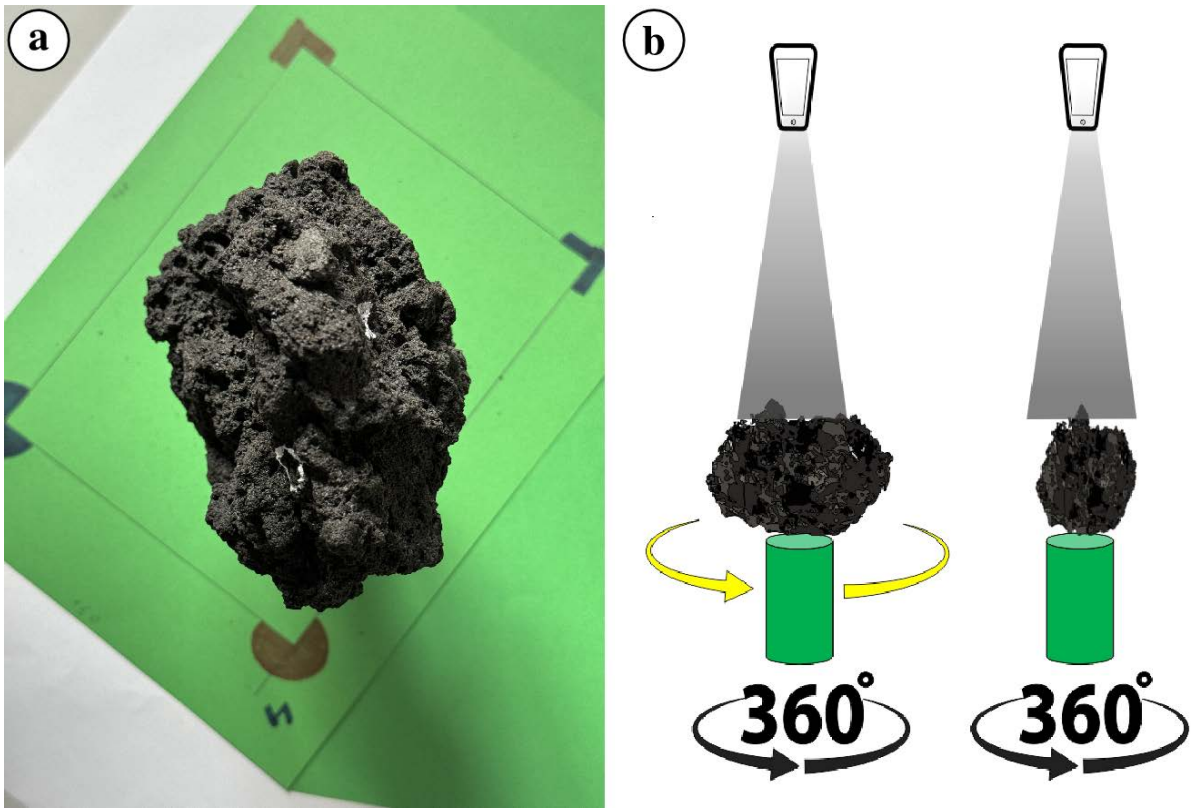

Figure 3. VPB collected in the field and analysed (a) in the INGV-OE laboratory above a sheet of green paper; (b) sketch of the shooting technique used in the INGV-OE laboratory.

be difficult to rotate the VPB in the field, especially in the case of a large size, the image acquisition procedure should be adapted to the context. In this case, the camera could be rotated around the sample, taking images from different angles and keeping the sample-camera distance as constant as possible. Markers should also be added to identify the relative position of the images and to correctly dimension the 3D model.

3.2 The VisualSFM-Meshlab processing method (VSFM)

We first processed the photos of the VPB using VisualSFM, a freeware software capable of generating 3D reconstruction of complex objects. Notably, 3D reconstructions obtained using this tool become increasingly detailed with a higher number of photographs taken from different perspectives (Ulman, 1979 and ccwu.me). VisualSFM is based on the Structure from Motion (SfM) technique (e.g. Furukawa et al., 2010; Lowe, 2004; Cignoni et al., 2008; Ranzuglia et al., 2009) which enables the extraction of scaled and geo-referenced dense point clouds. Once created, the point cloud obtained using the VPB photos was imported into Meshlab (MeshLab), a freely available software for processing and editing triangular meshes (Maggiordomo et al., 2021). The Surface Reconstruction was performed using the Screened Poisson function, while the Convex Hull command was used to create the convex envelope of the point cloud (i.e. the smallest convex set containing the set of points). We determined the scale factor needed to convert the dimensions of the 3D reconstruction from pixels to centimetres by comparing the linear distances between two graphic markers (a pair of markers) measured on both the model and the actual sample. Finally, we measured the three main axes (a, b, and c) and estimated the volume of the 3D reconstruction using the Meshlab software.

3.3 The Agisoft Metashape processing Method (AM)

The 3D reconstruction of the VPB sample was subsequently performed using Agisoft Metashape (v1.6.6, https://www.agisoft.com), a commercial software based on SfM. Image processing of all VBP photos (the two sets

of images corresponding to the top and bottom of the sample), at medium resolution resulted in a computational time of about 2 hours, and about 5 extra hours were needed to align the two individual 3D models (top and bottom of the sample) and scale the final model. To scale and align the two models we applied the same procedure used for the VSFM. In particular, we measured three and one pair of markers for the top and bottom sets of images, respectively. After cleaning the green background dots into the Metashape software, we merged the two point clouds and created a complete 3D model of the sample. The model was imported into the Meshlab software to derive the sample volume and into the Cloud Compare (v2.12.4) open-source software (https://www.danielgm.net/cc) to measure its maximum linear dimensions (a, b, and c).

3.4 The LiDAR Application (LiDAR-App)

Laser scanning technology (LiDAR) which has been implemented on the Pro versions of Apple iPads and iPhones since 2020, operates in the near-infrared (NIR) spectrum and emits a laser from a Vertical Cavity Surface Emitting Laser (VCSEL) in a 2D array (Khaldi et al., 2020). The VCSEL sensor is designed to measure the direct time-of-flight (dTOF) of pulses emitted with a Single Photon Avalanche Photodiode (Niclass et al., 2020). The maximum range of this sensor is 5 meters, and it emits an array containing 8 x 8 points that are diffracted into a 3 x 3 grid, which generates a total of 576 points. To acquire the point cloud necessary for the 3D reconstruction of our VPB sample, we used an iPhone 15 Pro and the 3D Scanner App by Laan Labs (version 2.0.17) which provides two scanning modes. One (LiDAR) does not allow parameters to be set and is recommended for scanning large objects. The other (LiDAR Advanced) allows the scanning parameters to be optimized in terms of confidence (low, medium, and high), range (from 0.3 m to 5.0 m), masking (none, object, and person), and resolution (5 mm to 20 mm). In addition, the software enables direct visualization of the acquired data and is equipped with measuring tools. We scanned the VBP sample using the following settings: high confidence, 5.0 m range, no masking, and a resolution of 5 mm. The 3D Scanner App directly measures the sample volume (LiDAR Volume Estimation LVE1). We imported the 3D model into the MeshLab software to refine the analysis and measure its volume (LiDAR Volume Estimation LVE2). Then the open-source software Cloud Compare (v2.12.4) (https://www.danielgm.net/cc) was used to measure its maximum linear dimensions (a, b, and c).

The acquisition and processing times of all the methods presented in this study are reported in Table 1.

Method	Photo Acquisition Time	Processing Time
VSFM	10 minutes	6-8 hours
AM	10 minutes	6-8 hours
LiDAR VE1	30 seconds	10 seconds
LiDAR VE2	30 seconds	15 minutes

Table 1. Photo acquisition and processing time using the different methods tested in this work.

3.5 The Eject! model

We estimated the ballistic trajectories of the VPB using the Eject! model, a trajectory calculator for ballistic clasts, freely available online (https://theghub.org/resources/4543). The software is written in Microsoft Visual Basic® and allows calculation of the trajectory of bombs/blocks, the maximum distance reached from the point of emission, the final fallout velocity, and the travel time (Mastin et al., 2001). The Eject! program requires the following input data: the initial clast ejection velocity (m/s), the ejection angle (degrees from horizontal), the vertical distance

between the takeoff point (in our case between the top of the Incandescent Jet Region, IJR often measured using a thermal camera), the landing point (m), the characteristics of the ejected particle (density in kg/m^3 and diameter in cm), the air drag coefficient, the atmospheric properties (wind velocity in m/s, temperature at sea level in °C, thermal gradient in °C/km) and the elevation of takeoff point (m above sea level). The input parameters fixed in all simulations are density, particle diameter, wind speed, and atmospheric properties, whereas the other parameters are based on the analysis of the 21 May 2023 eruption (De Beni et al., 2024). The input parameters, used to run the Eject! model, are listed in Table 2.

Input Data	Values
Initial ejection velocity (m/s)	100, 150
Ejection angle respect to horizontal (°)	45
Vertical distance take off-landing points (m)	500, 1000, 1500
Particle density (kg/m^3)	600
Diameter of equivalent sphere (cm)	12
Air drag coefficient (–)	0.5, 0.8, 1.0, variable
Wind velocity (m/s)	8
Sea level temperature (°C)	500, 1000, 1500
Thermal gradient (°C/km)	600
Elevation of take-off point a.s.l. (m)	12

Table 2. Input data used in the Eject! Model.

4. Results

4.1 The 3D reconstruction of VBP

In Fig. 4, we show the 3D reconstruction of the 21 May 2023 Etna's VBP and in Table 3 we summarize the corresponding geometrical parameters (lengths of a, b, and c axes, mean diameter, MD, and volume V) obtained with the different methodologies. The 'Reference Values' were measured using the caliper and Archimedes' principle. The difference between the measured and estimated parameters is lower than 12% for the mean diameter and ranges between 4.8% and 27.2% for the three main axes. All tested methods resulted in an overestimation of the VBP volume. Specifically, the less accurate volume estimate was obtained using the VSFM tool (estimated volume ~150% larger than reference volume) while the AM technique returned the most accurate result (estimated volume ~16% larger than reference volume). The LiDAR application (LVE2 method) produced an intermediate result (estimated volume ~86% larger than the reference volume). Moreover, we estimate the volume obtained by approximating the particle to an ellipsoid ($Ve = \frac{4}{3}\pi\frac{abc}{8}$) and from this value, we estimated the diameter (DV) of a sphere having the same volume V measured with each different methodology.

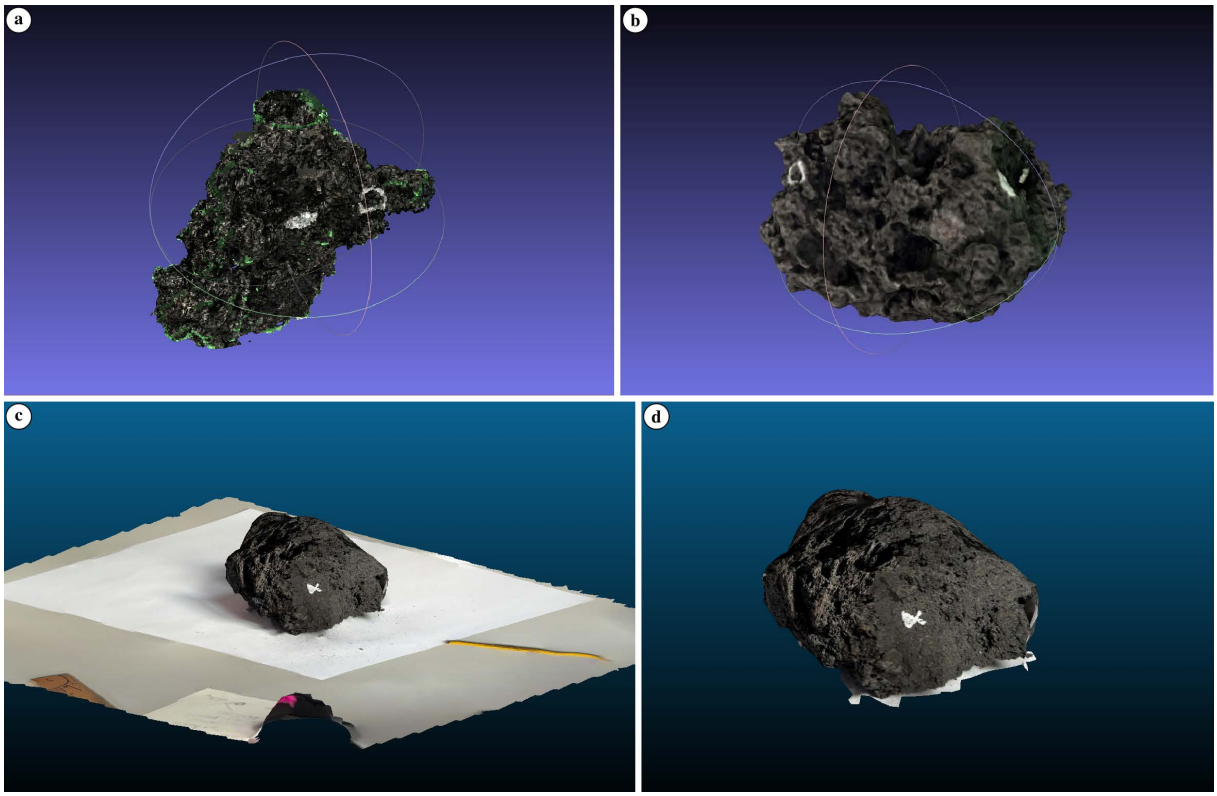

Figure 4. The point clouds of the VBP using the following methods: (a) VSFM, (b) AM, (c) LVE1 and (d) LVE2.

Method	a (cm)	b (cm)	c (cm)	MD (cm)	DV(cm)	V (cm^3)	V_e (cm^3)
Reference Value	**16.4**	**12.5**	**8.5**	**12.4**	**8.6**	**340.5**	**911.9**
VSFM	18.3 (11.6%)	11.8 (5.6%)	8.9 (4.7%)	13.0 (4.3%)	11.8 (37.2%)	860 (152.6%)	1005.7 (10.3%)
AM	14.0 (14.6%)	10.7 (14.4%)	10.4 (22.4%)	11.7 (6.2%)	9.2 (7%)	396.2 (16%)	815.3 (10.6%)
LiDAR VE1	15.6 (4.9%)	9.1 (27.2%)	8.3 (2.4%)	11.0 (11.8%)	11.8 (37.2%)	849.5 (150%)	616.6 (38.7%)
LiDAR VE2	15.6 (4.9%)	9.1 (27.2%)	8.3 (2.4%)	11.0 (11.8%)	10.6 (23.6%)	634.0 (86%)	616.6 (24.4%)

Table 3. Sizes (a, b, c); mean diameter (MD); diameter (DV) obtained considering a sphere having the volume (V) measured with different techniques; volume estimated by approximating the particle to an ellipsoid (V_e). The percentage values, in brackets, are the difference of each value to the corresponding reference value. Reference values for the size and volume (V) were measured using the caliber and the Archimedes principle, respectively. VSFM, AM, LVE1, and LVE2 are for VisualSFM-Meshlab, Agisoft Metashape, Lidar Volume Estimation 1, and Lidar Volume Estimation 2, respectively.

5. Discussion

5.1 Estimation of the VBP trajectory

We run the Eject! model using the derived from the weather data forecast database (Era5 reanalysis, https://cds.climate.copernicus.eu/cdsapp#!/dataset/reanalysis-era5-pressure-levels?tab=overview), last four rows in Table 2.

The vertical distance between the take-off and landing points is computed assuming an IJR height ranging between 1800 m and 2800 m above the crater rim (Mereu et al., 2020). Taking into account that ballistic clasts can be ejected at any point in the IJR, different take-off point elevations were considered between the SEC crater rim and the maximum IJR height (500 m, 1000 m, and 1500 m; Costa et al., 2023). In Fig. 5, we show how the variations of drag coefficient (Cd), ejection velocities, and vertical distances between take-off and landing points affect the horizontal distance reached by the clast of a diameter of about 12 cm. Overall, we note that an increase in the ejection velocity (from 100 m/s to 150 m/s) produces an increase in the horizontal distance reached by the clast. This increase is in the order of 100 m if the air drag coefficient is fixed at values of 0.5, 0.8, and 1 (Fig. 5a-c) and much higher when we consider a variable Cd (Fig. 5d). When the Cd is variable the model assumes different types of clast shapes, like spheres, cubes, and artillery, to estimate the variability of Cd throughout the trajectory (Costa et al., 2023). Indeed, in these conditions, the horizontal distance increases by more than 400 m when we increase the ejection velocity from 100 m/s to 150 m/s. The trajectory that best fits the actual vent-VBP distance was obtained using the following conditions: Cd = 0.5 or variable, ejected velocity equal to 150 m/s, and vertical distance between the takeoff point and the landing point equal to 1500 m or 500 m, as shown in Fig. 6a (cyan line) and Fig. 6d (yellow line), respectively.

Subsequently, we estimated the variability of ballistic trajectories, considering the diameters md = 11, 11.7, 12.4, and 13 cm and DV = 8.6, 9.2, 10.6 and 11.8 cm reported in Table 3. We also assume Cd = 0.5 and variable Cd, the ejected velocity equals 100 m/s and 150 m/s, and the vertical distance between the take-off point and the landing points equals 1500 m and 500 m, respectively (Fig. 6). These conditions correspond to the best-fit parameters

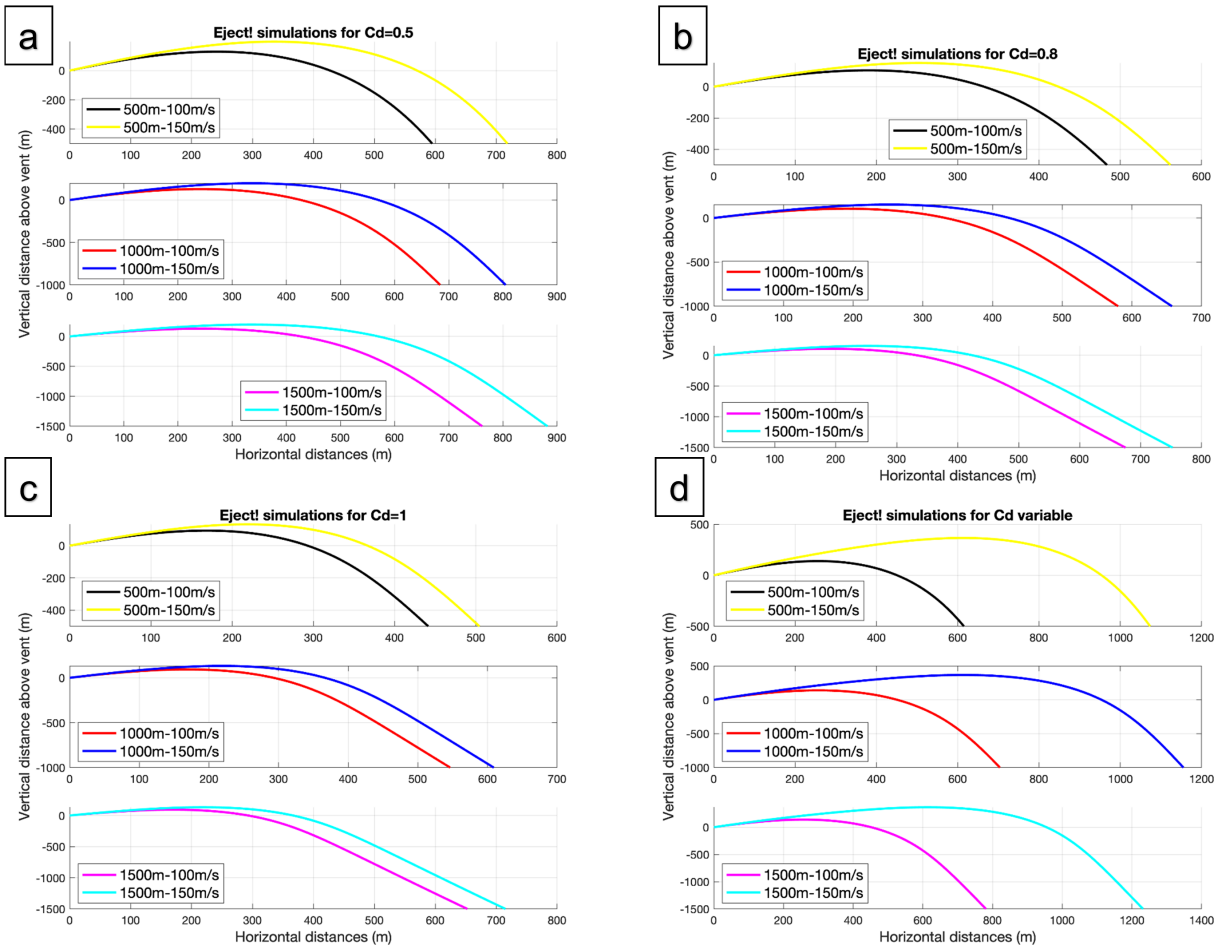

Figure 5. Trajectories of ballistics obtained with the Eject! software for different drag coefficients (Cd = 0.5, 0.8, 1 and variable; panels (a), (b), (c), and (d), respectively). Different colours represent the trajectories obtained for variable ejection velocities (100 m/s and 150 m/s) and vertical distances between take-off and landing points (500 m, 1000 m and 1500 m). The ballistic trajectories are in function of the height difference between the ground level and the incandescent jet region (IJR, i.e. the vertical distance above the vent; Mereu et al., 2020) and the horizontal distance from the vent for a bomb with a diameter of about 12 cm.

obtained in the previous simulations (Fig. 5). The simulations show the VBP trajectories, obtained by considering the diameters obtained with the different techniques (Table 3). It is notable that when Cd is variable, there is a greater difference in the trajectory. In fact, considering DV, the maximum difference between the maximum distance reached by the VBP is about 350 m, considering DV = 8.6 cm (reference value in Table 3) and DV = 11.8 cm, whereas for MD the difference is 250 m. Instead for Cd = 0.5 and for both DV and MD, the difference is least than 100 m. Our results show that an error of 350 m, due to a different way to estimate the particle size, should be considered in the estimation of the maximum distance reached by the VBP.

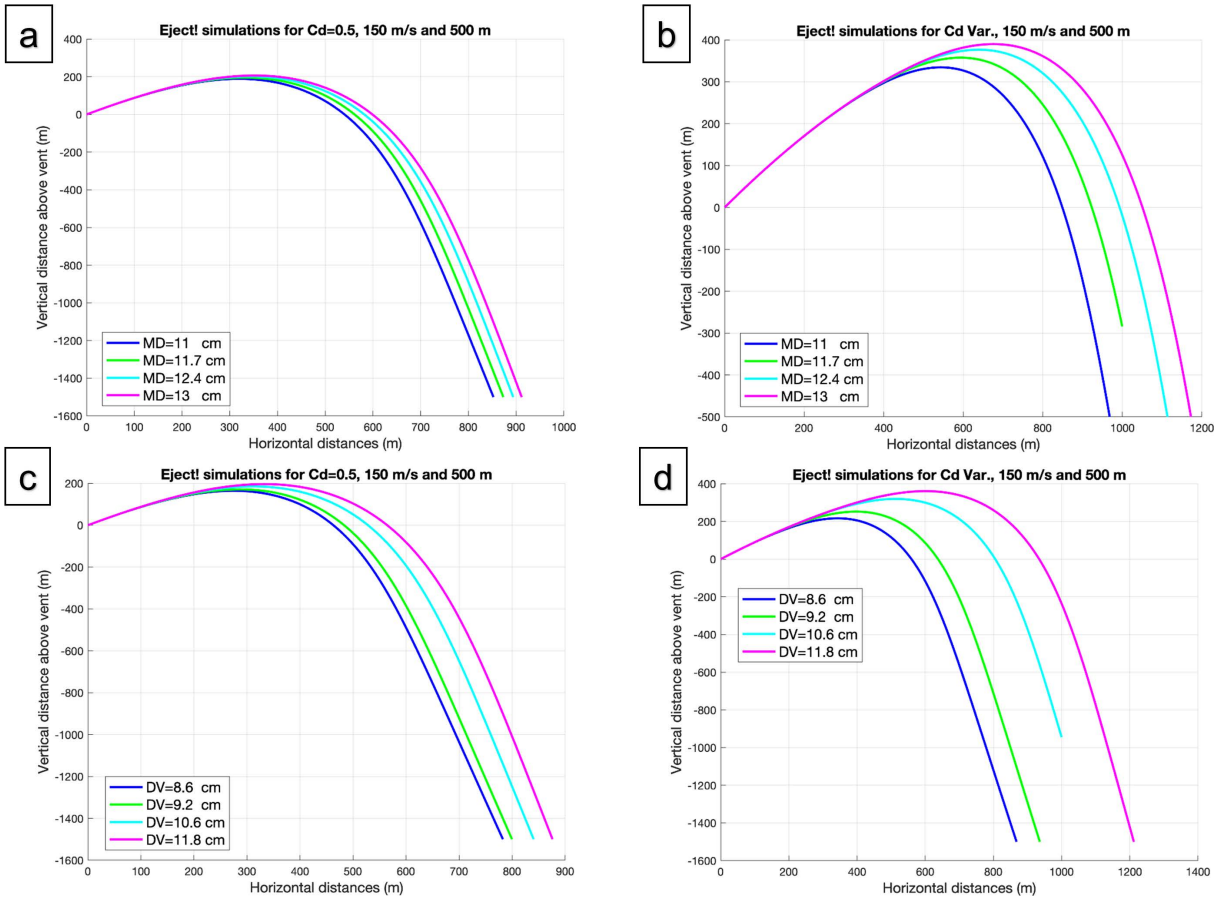

Figure 6. Trajectories of ballistics obtained with the Eject! tool considering Cd = 0.5 (in the left) and a variable Cd (in the right), the initial ejection velocity of 150 m/s and the vertical distance between take-off and landing points equals to 1500 m and 500 m. Different colours represent the different MD diameters (Table 3) in the upper panels and DV diameter.

5.2 Comparison of different methodologies

In this work we measured the size and volume of a VBP ejected during an explosive eruption at the Etna volcano (Italy). We performed 3D reconstructions of the VBP through photogrammetric processing with both freely available and commercial software (VSFM and AM, respectively). Additionally, we tested the capability of LiDAR applications (LVE1 and LVE2) embedded in an iPhone to obtain similar reconstructions. We used these 3D reconstructions to estimate the VBP volume and mean diameter and compared the results with reference values derived by physical measurement of the VBP sample. We found that differences between the estimated and measured mean diameters are smaller than 12% while greater differences are observed in the volume estimates (Table 3). Overall, all methods result in volume overestimation compared to the value obtained using Archimedes' principle (AP, Table 3). Specifically, the volumes obtained using the VSFM and LVE1 methods are more than twice the actual volume. The LVE2 method returns slightly better results (estimated volume about 86% larger than the reference

volume; Table 3). The discrepancy between the volume estimated using the AM and the reference volume is the lowest (about 16%; Table 3) thus suggesting that the commercial software is capable of capturing the irregular shape of highly porous volcanic particles. However, we highlight that the 3D reconstruction, and thus the corresponding differences among measured and estimated geometries, could return better results for samples characterized by lower porosity and a more regular shape compared to our sample.

Each of the tested methods has strengths and weaknesses during image acquisition and processing. For example, the methods based on Structure from Motion (SfM) reconstructions (i.e., VSFM and AM) require optimal illumination conditions, which might be difficult to fulfil in the field. Additionally, the SfM-based methods need the application and measurement of markers, which can be challenging for large-size samples, and data processing is complex and time-consuming (one working day for both the VSFM and AM methods), particularly when dealing with highly irregular shapes. Moreover, VSFM and AM are easy to apply, requiring only a camera or a mobile phone for capturing images and a marker to draw the points on the sample. However, the post-processing stage is time-intensive and requires significant effort. Figure 7 shows an example of 3D shape reconstruction of a VBP from Etna using the VSFM. The reconstruction was successful but required adding more markers on the VBP surface to ensure accuracy. While this method shows good potential, analyzing larger bombs could present challenges due to the computational demands of processing a significantly higher number of images.

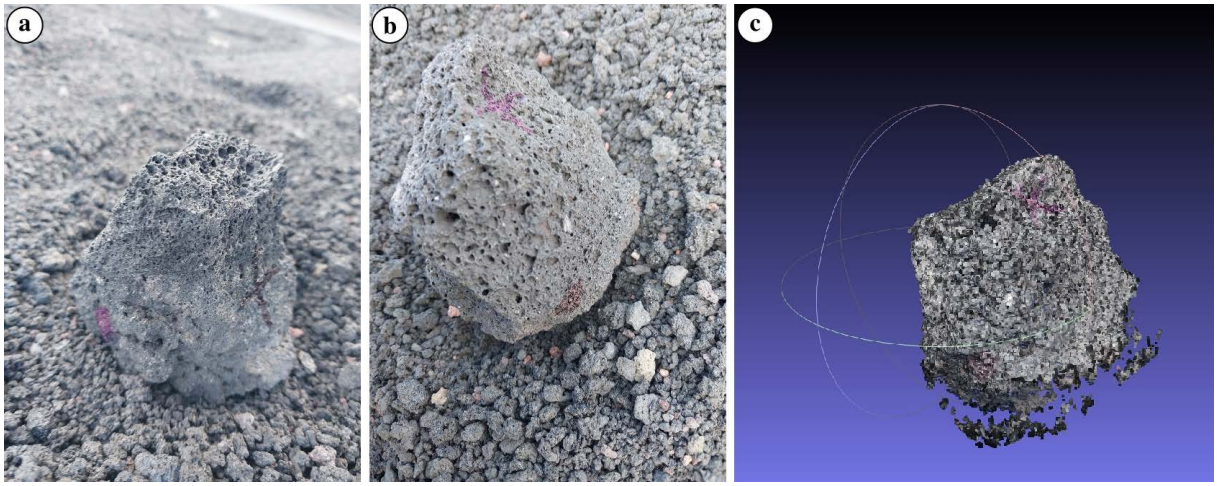

Figure 7. An example of a bomb analysed in the field at about 4.5 km south from the volcano summit adding different markers (a) and (b) to allow (c) the 3D reconstruction using the VSFM.

In contrast, the processing time can be significantly reduced using the LiDAR application, as shown in Table 2.

In the LVE2 method, the LiDAR sensor directly acquires depth data using laser pulses, while the camera simultaneously acquires images intended for 3D model texturing. This approach allows a 3D model to be generated in real-time, reducing the total acquisition time to a few minutes. Subsequent processing is limited to applying the textures, acquired along with the depth data, to the already generated 3D model. This approach significantly optimizes the overall workflow. The LiDAR application, particularly the LVE2, is the most promising for the following reasons: i) it does not require good weather conditions; ii) it does not need markers on the VBPs; iii) it gives the lower uncertainty for the volume estimation compared to other methods (except the AM method); iv) it is a very fast method, suitable for reducing the time spent by volcanologists near potentially dangerous active summit craters. However, the LiDAR App is currently available only on iPhones. Hopefully, this technology will become available on a wider range of cheaper and portable devices in the future. By comparing the different techniques, it is possible to determine the most suitable method based on specific needs and available tools. For example, for high-speed surveying and processing resulting in medium accuracy, LIDAR is a good choice. However, if more time is available and higher accuracy is needed, AM is preferable. Our study shows that if a LiDAR App is not available or the available time is short, the estimation of three main axes remains the fastest method to represent the shape of VBPs.

These methods can provide valuable insights into eruptive dynamics by estimating how geometric shapes (e.g., cube, cylinder, spheroid) capture the main morphologies of VBPs, thereby reducing uncertainty in simulating

ballistic trajectories. Importantly, we have observed that volume represents the most important parameter for the VBP trajectory simulations as the differences in particle volume (and in turn in particle diameter) found in this study can cause variations of up to about 350 m in the horizontal distance reached by VBPs (Fig. 7). In the context of volcanic risk management, these discrepancies should be considered during the estimation of the associated hazards (Costa et al., 2023).

Data availability statement. Images and analysis can be requested by the authors.

Acknowledgements. The work was funded by the INGV-MIUR project Pianeta Dinamico "Working Earth" Sub-project VT – DYNAMO-2023, by the Sub-project SAFARI-2023 and PANACEA project, and partially by the Space It Up project. We thank technicians and technologists who take care of the INGV-OE camera network, and the volcanologists of INGV-OE who regularly collect data during volcanic events. We also thank the administrative and technical support of INGV-OE that allows us to collect and analyze data. This work was also funded by the Italian Presidenza del Consiglio dei Ministri – Dipartimento della Protezione Civile (DPC), All. A. This paper does not necessarily represent DPC official opinion and policies.
Finally, we thank D. Andronico e L. Miraglia who allowed us to use the sedimentological laboratory of INGV-OE.

References

Bagheri, G. and C. Bonadonna (2016). On the drag of freely falling non-spherical particles, Powder Technol., 301, 526-544, doi:10.1016/j.powtec.2016.06.015.

Bonadonna, C., R. Genco, M. Gouhier, M. Pistolesi et al. (2011). Tephra sedimentation during the 2010 Eyjafjallajökull eruption (Iceland) from deposit, radar, and satellite observations, J. Geophys. Res., 116, B12202, doi:10.1029/2011JB008462.

Bisson, M., C. Spinetti, R. Gianardi, K. Strehlow et al. (2023). High-resolution mapping and dispersion analyses of volcanic ballistics emitted during the 3rd July 2019 paroxysm at Stromboli, Sci. Rep., 13, 13465, doi:10.1038/s41598-023-39600-w.

Blong, R. J. (1984). Hazards produced by volcanic eruptions, in Volcanic Hazards, R. J. Blong (Editor), Academic Press, San Diego, 14-69, ISBN:978-0-12-107180-6.

Brown, S. K., S. F. Jenkins, R. S. J. Sparks, H. Odbert et al. (2017). Volcanic fatalities database: analysis of volcanic threat with distance and victim classification, J. Appl. Volcanol., 6, 1, doi:10.1186/s13617-017-0067-4.

Calvari, S. and G. Nunnari (2022). Comparison between Automated and Manual Detection of Lava Fountains from Fixed Monitoring Thermal Cameras at Etna Volcano, Italy, Remote Sens., 14, 2392, doi:10.3390/rs14102392.

Chester, D. K., A. M. Duncan, J. E. Guest and C. R. J. Kilburn (1985). Mount Etna, The Anatomy of a Volcano, Chapman & Hall, London, 404, ISBN:9780804713085.

Cioni, R., D. Andronico, L. Cappelli, A. Aravena et al. (2024). Products and dynamics of lava-snow explosions: The 16 March 2017 explosion at Mount Etna, Italy, Geol. Soc. Am. Bull., 136, 5-6, 2325-2342, doi:10.1130/B37102.1.

Cignoni, P., M. Callieri, M. Corsini, M. Dellepiane et al. (2008). MeshLab: an Open-Source Mesh Processing Tool, Sixth Eurographics Italian Chapter Conference, Salerno, Italy, 129-136, doi:10.2312/LocalChapterEvents/ItalChap/ItalianChapConf2008/129-136.

Coltelli, M., L. Miraglia and S. Scollo (2008). Characterization of shape and terminal velocity of tephra particles erupted during the 2002 eruption of Etna volcano, Italy, Bull. Volcanol., 70, 1103-1112, doi:10.1007/s00445-007-0192-8.

Costa, G., L. Mereu, M. Prestifilippo, S. Scollo et al. (2023). Modeling the Trajectories of Ballistics in the Summit Area of Mt. Etna (Italy) during the 2020-2022 Sequence of Lava Fountains, Geosci., 13, 145, doi:10.3390/geosciences13050145.

De Beni, E., C. Proietti, S. Scollo, M. Cantarero et al. (2024). A Hidden Eruption: The 21 May 2023 Paroxysm of the Etna Volcano (Italy), Remote Sens., 16, 1555, doi:10.3390rs16091555.

Dellino, P., D. Mele, R. Bonasia, G. Braia et al. (2005). The analysis of the influence of pumice shape on its terminal velocity, Geophys. Res. Lett., 32, 21, L21306, doi:10.1029/2005GL023954.

Dioguardi, F., D. Mele and P. Dellino (2018). A new one-equation model of fluid drag for irregularly shaped particles valid over a wide range of Reynolds number, J. Geophys. Rese. Solid Earth, 123, 144-156, doi:10.1002/2017JB014926.

Ersoy, O. (2010). Surface area and volume measurements of volcanic ash particles by SEM stereoscopic imaging, J. Volcanol. Geotherm. Res., 190, 3-4, 290-296, doi:10.1016/j.jvolgeores.2009.12.006.

Fitzgerald, R. H., B. M. Kennedy, T. M. Wilson, G. S. Leonard et al. (2017). The Communication and Risk Management of Volcanic Ballistic Hazards, Advances in Volcanology, Springer International Publishing, 121-147, doi:10.1007/11157_2016_35.

Fitzgerald, R., K. Tsunematsu, B. Kennedy, E. Breard et al. (2014). The application of a calibrated 3D ballistic trajectory model to ballistic hazard assessments at Upper Te Maari, Tongariro, J. Volcanol. Geotherm. Res., 286, 248-262, doi:10.1016/j.jvolgeores.2014.04.006.

Fitzgerald, R. H., B. M. Kennedy, C. Gomez, T. M. Wilson et al. (2020). Volcanic ballistic projectile deposition from a continuously erupting volcano: Yasur Volcano, Vanuatu, Volcanica, 3, 2, 183-204, doi:10.30909/vol.03.02.183204.

Furukawa, Y. and J. Ponce (2010). Accurate, dense, and robust multiview stereopsis, IEEE Trans. Pattern Anal. Mach. Intell., 32, 8, 1362-1376, doi:10.1109/TPAMI.2009.161.

Ganser, G. (1993). A Rational Approach to Drag Prediction of Spherical and Non-Spherical Particles, Powder Technol., 77, 143-152, doi:10.1016/0032-5910(93)80051-B.

Guest, J. E., J. B. Murray, C. R. J. Kilburn, R. M. C. Lopes et al. (1980). An eyewitness account of the Bocca Nuova explosion of 12 September 1979, in United Kingdom Research on Mount Etna A. T. Huntingdon (Editor), Royal Soc. London, 1977-1979, 44-46.

Guffanti, M., J. W. Ewert, G. M. Gallina, G. J. S. Bluth et al. (2005). Volcanic-Ash Hazard to Aviation during the 2003-2004 Eruptive Activity of Anatahan Volcano, Commonwealth of the Northern Mariana Islands, J. Volcanol. Geotherm. Res., 146, 241-255, doi:10.1016/j.jvolgeores.2004.12.011.

Gurioli, L., A. Harris, L. Colò, J. Bernard et al. (2013). Classification, landing distribution, and associated flight parameters for a bomb field emplaced during a single major explosion at Stromboli, Italy, Geology, 41, 5, 559-562, doi:10.1130/g33967.1.

Heiken, G. and K. H. Wohletz (1985). Volcanic Ash, University of California Press, Berkeley, 245.

Khaldi, A., E. Daniel, L. Massin, C. Kärnfelt et al. (2020). A laser emitting contact lens for eye tracking, Sci. Rep., 10, 14804, doi:10.1038/s41598-020-71233-1.

Kieffer, G. (1979). L'explosion meurtrière du 12 septembre 1979 de l'Etna, Comptes Rendus de l'Académie des Sciences Paris, Série D, 289, 1013-1016.

Liu, E. J., K. V. Cashman and A. C. Rust (2015). Optimising shape analysis to quantify volcanic ash morphology, GeoResJ, 14-30, doi:10.1016/j.grj.2015.09.001.

Lowe, D. G. (2004). Distinctive image features from scale-invariant keypoints, Int. J. Comput. Vis., 60, 2, 91-110, doi:10.1023/B:VISI.0000029664.99615.94.

Maggiordomo, A., P. Cignoni and M. Tarini (2021). Texture Defragmentation for Photo-Reconstructed 3D Models, Computer Graphics Forum, 40, 2, doi:10.1111/cgf.142615.

Mastin, L. G. (2001). A Simple Calculator of Ballistic Trajectories for Blocks Ejected during Volcanic Eruptions, Technical Reports, 1-45, U. S. Geological Survey, Reston, VA, USA, doi:10.3133/ofr0145.

Minakami, T. (1942). On the distribution of volcanic ejecta (Part I.): The distributions of volcanic bombs ejected by the recent explosions of Asam, Bulletin of the Earthquake Research Institute, Tokyo Imperial University, 20, 65-92.

Mereu, L., S. Scollo, C. Bonadonna, V. Freret-Lorgeril et al. (2020). Multisensor characterization of the incandescent jet region of lava fountain-fed tephra plumes, Remote Sens., 12, 21, 3629, doi:10.3390/rs12213629.

Mereu, L., S. Scollo, C. Bonadonna, F. Donnadieu et al. (2022), Ground-Based Remote Sensing and Uncertainty Analysis of the Mass Eruption Rate Associated with the 3-5 December 2015 Paroxysms of Mt. Etna, IEEE J. Sel. Top. Appl. Earth Obs., 15, 504-518, doi:10.1109/JSTARS.2021.3133946.

Mereu, L., S. Scollo, A. Garcia, L. Sandri et al. (2023). A new radar-based statistical model to quantify mass eruption rate of volcanic plumes, Geophys. Res. Lett., 50, e2022GL100596, doi:10.1029/2022GL100596.

Murray, J. B. (1980). The Bocca Nuova: its history and possible causes of the September 1979 explosion, in United Kingdom Research on Mount Etna 1977-1979, A. T. Huntingdon (Editor), Royal Soc. London, 46-50.

Niclass, L., A. Shpunt, G. Agranov, M. C. Waldon et al. (2020). Imaging System with Synchronized Scan and Sensing, USA patent US 10,795,001 B2.

Pioli, L., M. Palmas, B. Behncke, E. De Beni et al. (2022). Quantifying Strombolian Activity at Etna Volcano, Geosci., 12, 163, doi:10.3390/geosciences12040163.

Proietti, C., E. De Beni, M. Cantarero, T. Ricci et al. (2023). Rapid provision of maps and volcanological parameters: quantification of the 2021 Etna volcano lava flows through the integration of multiple remote sensing techniques, Bull. Volcanol., 85, 58, doi:10.1007/s00445-023-01673-w.

Proietti, C., E. De Beni and M. Cantarero (2024). One hundred lava flows of Mt Etna, Italy: July 2019-December 2023 update, J. Maps, doi:10.1080/17445647.2024.2380899.

Ranzuglia, G., M. Callieri, M. Dellepiane, P. Cignoni et al. (2012). Efficient and Flexible Sampling with Blue Noise Properties of Triangular Meshes, IEEE Trans. Vis. Comput. Graph., 18, 6, 914-924, doi:10.1109/TVCG.2012.34.

Reynolds, O. (1883). An Experimental Investigation of the Circumstances Which Determine Whether the Motion of Water Shall Be Direct or Sinuous, and of the Law of Resistance in Parallel Channels, Philos. Trans. R. Soc., 174, 935-982, doi:10.1098/rstl.1883.0029.

Saxby, J., A. Rust, F. Beckett, K. Cashman et al. (2020). Estimating the 3D shape of volcanic ash to better understand sedimentation processes and improve atmospheric dispersion modelling, Earth Planet. Sci. Lett., 534, doi:10.1016/j.epsl.2020.116075.

Stokes, G. (1851). On the Effect of the Internal Friction of Fluids on the Motion of Pendulums, Trans. Cambridge Philos. Soc., 9, 8-106.

Swanson, D. A., S. P. Zolkos and B. Haravitch (2012). Ballistic blocks around Kılauea Caldera: Their vent locations and number of eruptions in the late 18th century, J. Volcanol. Geotherm. Res., 231-232, 1-11, doi:10.1016/j.jvolgeores.2012.04.008.

Taddeucci, J., M. A. Alatorre-Ibargüengoitia, O. Cruz-Vázquez, E. D. Bello et al. (2017). In-flight dynamics of volcanic ballistic projectiles, Rev. Geophys., 55, 3, 675-718, doi:10.1002/2017rg000564.

Tsunematsu, K., B. Chopard, J. L. Falcone and C. Bonadonna (2014). A numerical model of ballistic transport with collisions in a volcanic setting, Comput. Geosci., 63, 62-69, doi:10.1016/j.cageo.2013.10.016.

Ullman, S. (1979). The interpretation of structure from motion, Proc. R. Soc. Lond. B. Biol. Sci., 203, 1153, 405-426, doi:10.1098/rspb.1979.0006.

***CORRESPONDING AUTHOR: Simona SCOLLO**,
Istituto Nazionale di Geofisica e Vulcanologia, Osservatorio Etneo, Catania, Italy
e-mail: simona.scollo@ingv.it